Journal of Materials Chemistry C

ROYAL SOCIETY OF CHEMISTRY

PAPER

View Article Online
View Journal | View Issue

Cite this: J. Mater. Chem. C, 2021, 9, 982

First-principles study of aziridinium tin iodide perovskites for photovoltaics

Qiang Teng,[ab] Tingting Shi,[c] Chengwei Liao[a] and Yu-Jun Zhao *[ad]

Received 16th August 2020,
Accepted 6th December 2020

DOI: 10.1039/d0tc03902k

rsc.li/materials-c

Solar cells with organic–inorganic lead halide perovskites have attracted great attention in the last decade. Herein, we propose lead-free halide perovskite $(CH_2)_2NH_2SnI_3$, as well as alloys $(CH_2)_2NH_2SnI_{3-x}Br_x$, to avoid the toxicology of lead element. We find that the perovskite $(CH_2)_2NH_2SnI_3$ has much better stability than $CH_3NH_3PbI_3$ and possesses a band gap of 1.06 eV. Meanwhile, the alloy $(CH_2)_2NH_2SnI_2Br$ has an ideal band gap of 1.31 eV for photovoltaics. The alloy $(CH_2)_2NH_2SnI_{3-x}Br_x$ is proved to have higher optical absorption than $CH_3NH_3PbI_3$ in general. We thus propose that the lead-free perovskite $(CH_2)_2NH_2SnI_3$ and alloys $(CH_2)_2NH_2SnI_{3-x}Br_x$ are probably excellent candidates for stable and high-performance photovoltaic absorber materials.

1. Introduction

Organic–inorganic hybrid halide perovskite solar cells (PSCs) are a promising photovoltaic (PV) technology, as lead (Pb)-based hybrid perovskite solar cells (HPSCs) have achieved impressive power conversion efficiencies (PCEs) over 25.2% since the first report in 2009.[1,2] However, the long-term instability and toxicity of lead in the PSCs still need to be addressed for further commercialization applications of them. Partial or full substitution of the organic cations, efficient encapsulation and interfacial functionalization are powerful ways to improve the stability of the hybrid perovskites.[3–6]

Moreover, one of the most feasible strategies to address the toxic issue is to replace Pb with tin (Sn), which is also from Group IV. Considering its electron configuration of ns^2np^2 and coordination geometry akin to Pb, the Sn-based perovskite should possess largely inherent semiconducting properties of the pristine Pb-based counterpart.[7,8] In addition, the Sn-based perovskite family has also been reported to possess lower band gaps than those of the pristine Pb-based family,[9] which not only can broaden the applications of organic–inorganic hybrid perovskites in tandem solar cells for further enhancing PCEs[10,11] but can also facilitate the development of photosensors/photoconductors operating in the infrared region.[12] However, few systematic biological studies have shown that Sn may pose more danger to the environment and may not be a cost-effective alternative.[13,14] Nevertheless, the latest studies have demonstrated that tin perovskites are significantly less bioavailable than lead-based perovskites.[15,16] Thus, to some extent, tin may be a safer alternative to replace lead for lead-based halide perovskites.

However, the development of efficient pure Sn-based PSCs is hindered by the chemical instability of the Sn^{2+} element. Sn, with a weakened inert pair effect compared to the heavier Pb in Group IV, has strong propensity to be oxidized to Sn^{4+}. Consequently, the pure Sn-based perovskites will lose suitable semiconducting properties for photovoltaic applications, leading to poor device reliability and reproducibility.[7,17] To mitigate this troublesome Sn oxidation, one prevailing method adopted recently is to constitute Pb–Sn binary perovskites, for which the amount of Sn incorporated in the perovskite lattice is less and the superior semiconducting properties of the pristine $APbI_3$ ($A = Cs^+$, methylammonium (MA^+) or formamidinium (FA^+)) can be retained for realizing high performance.[10,18] However, in contrast to Pb–Sn binary perovskites, the development of efficient $ASnX_3$ PSCs needs much more elaborate efforts.[19,20]

In general, to effectively retard Sn oxidation for achieving efficient pure $ASnX_3$ PSCs, precise control of the precursor solution state and the resulting film morphology is a prerequisite.[21,22] Recently, SnF_2 has been demonstrated as an effective additive to prevent the oxidation of Sn^{2+} and has been widely used for Sn-based film deposition. Lately, by coupling the SnF_2 additive with morphological engineering, Seok and co-workers have reported an efficient and stable (with encapsulation) conventional n–i–p $FASnI_3$ PSC with a PCE of 4.8%.[22] Soon after, Yan and co-workers employed a similar deposition method to realize an improved PCE of 6.22% in an inverted

[a] Department of Physics, South China University of Technology, Guangzhou, Guangdong 510640, China. E-mail: zhaoyj@scut.edu.cn; Fax: +86-20-87112837; Tel: +86-20-87110426
[b] School of Science, East China University of Technology, Nanchang, Jiangxi 330013, China
[c] Siyuan Laboratory, Guangzhou Key Laboratory of Vacuum Coating Technologies and New Energy Materials, Department of Physics, Jinan University, Guangzhou, Guangdong 510632, China
[d] Key Laboratory of Advanced Energy Storage Materials of Guangdong Province, South China University of Technology, Guangzhou, Guangdong 510640, China

p–i–n device configuration,[23] reflecting the importance of device engineering on Sn-based PSCs. Very recently, Diau and co-workers realized a robust Sn-based PSC with a PCE of about 10%.[24]

Earlier research suggested that $CsSnI_3$ exhibits p-type metallic behavior with low carrier density,[25] and therefore it is not suitable for photovoltaic applications. Moreover, compared with $MASnI_3$, $FASnI_3$ crystals are much better for air stability and their conductivity can be tuned from p-type to intrinsic by varying the growth conditions.[8,26] Thus, $FASnI_3$ has much better performance than $MASnI_3$ in photovoltaic applications. $FASnI_3$, however, has a slightly larger band gap (1.41 eV)[27] than the optimum value (1.30 eV)[28] for single junction solar cells and thus its maximum theoretically efficiency is much lower than that of $MAPbI_3$ PSC.

Recently, Zheng *et al.* reported that the ionization energy of an A site molecule is a very important factor that determines the thermodynamical stability of $APbI_3$ hybrid halide perovskites and the lower ionization energy of the cations favors a more stable perovskite structure.[29] Subsequently, they proposed a much lower ionization energy organic molecule $((CH_2)_2NH_2)^{2+}$ (AZ) than that of CH_3NH_3 (MA) and $HC(NH_2)_2$ (FA) to be used as the organic cation at the A site of hybrid halide perovskites, which demonstrated that the low ionization energy of organic radical $(CH_2)_2NH_2$ decreases the reaction enthalpy of forming the corresponding perovskite, and this lower reaction enthalpy renders a much better stability of $AZPbI_3$ than $MAPbI_3$ and $FAPbI_3$.[30]

Herein, we propose a lead-free halide perovskite $(CH_2)_2NH_2SnI_3$ ($AZSnI_3$) as well as related alloys $AZSnI_{3-x}Br_x$, for stable and high-performance photovoltaic absorber materials, based on first-principles calculations. We demonstrate that $AZSnI_3$ and alloys $AZSnI_{3-x}Br_x$ possess appropriate band gaps and have higher optical absorption than $MAPbI_3$ in general.

2. Computational details

All calculations are performed using density functional theory (DFT) with the projected augmented wave (PAW) method as implemented in the Vienna *ab initio* simulation package (VASP).[31–33] The valence electron configurations involved in the calculations are chosen as H ($1s^1$), C ($2s^22p^2$), N ($2s^22p^3$), Sn ($4d^{10}5s^25p^2$), I ($5s^25p^5$) and the exchange–correlation functional is described by the generalized gradient approximation (GGA) *via* the Perdew–Burke–Ernzerhof (PBE) functional.[34] Because van der Waals (vdW) effects are important for the polymorphism of $MAPbI_3$,[35] these can be extended for other types of organic–inorganic hybrid halide perovskites. Thus, the PBE + vdW (D3)[36] exchange–correlation functional is also adopted in our calculations. Here, we choose the cubic $AZSnI_3$ with a space group of $Pm\bar{3}m$ for simulation, as the difference of our calculated formation enthalpies between its cubic, tetragonal, orthorhombic phases is within 10 meV per formula unit (*cf.* Section 3.1). The lattice parameters as well as the atomic positions are fully relaxed until the Hellmann–Feynman force on each atom is within 0.01 eV $Å^{-1}$. A Monkhorst–Pack[37] scheme $6 \times 6 \times 6$ and the $8 \times 8 \times 8$ Γ-centered k-point mesh over the first Brillion were used for the calculation of the structural optimization and electronic/optical properties, respectively. The wave function is expanded by plane-waves with an energy cut-off at 520 eV. Our previous investigation showed that the effect of spin–orbit coupling (SOC) is quite small on the calculated bandgap of the Sn-based halide perovskite ($FASnI_3$), unlike that of the Pb-based perovskite.[26] The calculated bandgap of $FASnI_3$ is narrowed to 0.21 eV when SOC is considered. Thus, to balance the computational cost and computational accuracy in this work, Heyd–Scuseria–Ernzerhof (HSE06)[38] based calculations are performed. Taking $CsSnI_3$ as a reference to correct the HSE06 band gap by varying the mixing rate (μ) of the Hartree–Fock exchange potential with the experimental band gap (1.30 eV),[39,40] $\mu = 0.30$ is in excellent agreement with the experiment value, yielding the calculated bandgap of 1.30 eV. Therefore, the above set is also employed for the calculation of the electronic structure in this work.

Based on the accurate electronic structure, the imaginary part $\varepsilon_2(\omega)$ of the dielectric function dependence on the incidence optical frequency can be acquired, and the real part $\varepsilon_1(\omega)$ can be estimated through Kramers–Kronig transformation. The optical absorption coefficient $I(\omega)$ can be obtained according to the following equation:[41]

$$I(\omega) = \sqrt{2}\omega\left[\sqrt{\varepsilon_1^2(\omega) + \varepsilon_2^2(\omega)} - \varepsilon_1(\omega)\right]^{1/2} \quad (1)$$

For the defect calculations, a $3 \times 3 \times 3$ supercell containing 351 atoms is employed, with the corresponding Brillouin zone sampled by the Γ point. The atomic coordinates are relaxed until the force on each atom is below 0.05 eV $Å^{-1}$. The defect formation energy $\Delta H(\alpha,q)$ has been calculated using the following equation:[42]

$$\Delta H(\alpha, q) = E(\alpha, q) - E_h + \sum_i n_i(E_i + \Delta\mu_i) + q[E_v + E_F] \quad (2)$$

where $E(\alpha,q)$ and E_h are the total energies of a supercell containing the defect in the charge state q and a perfect host supercell, respectively. n_i indicates the number of i atoms added ($n_i > 0$) or removed ($n_i < 0$) when a defect is formed. $\Delta\mu_i$ is the relative chemical potential of i depending on the experimental conditions and E_i is the total energy of i as the pure elemental solid or molecule. E_v is the valence band maximum (VBM) and E_F is the Fermi energy referred to the VBM. The transition level of the defect $\varepsilon(q/q')$ is defined as the Fermi level at which the formation energies of defect α with charge states q and q' are equal[42]

$$\varepsilon(q/q') = [\Delta H(\alpha,q) - \Delta H(\alpha,q')]/(q' - q), \quad (3)$$

where $\Delta H(\alpha,q)$ and $\Delta H(\alpha,q')$ are the formation energies of defect α with charge states q and q', respectively.

3. Results and discussion

3.1. Structural properties

The main issues of popular halide perovskite $MAPbI_3$ with an excellent PV performance are its poor structural and chemical stability along with the serious issue of lead (Pb) toxicity. Structural stability could be defined as the ability of a material to exist in a perovskite phase with suitable PV performance with the limitations of temperature and pressure.[43] Here, we have considered the cubic, tetragonal, orthorhombic structures of $AZSnI_3$. Previous results suggested that moisture or oxygen in the environment causes the poor stability of $MAPbI_3$ films,[44,45] whereas the subsequent theoretical analysis suggested that the material is intrinsically thermodynamically unstable with respect to phase separation into PbI_2 and MAI.[46] Herein, decomposition enthalpies (ΔH_d) of the considered three types of $AZSnI_3$ are calculated by the following decomposition reaction equation

$$AZSnI_3 \rightarrow AZI + SnI_2 \quad (4)$$

and the corresponding enthalpy

$$\Delta H_d = E_{tot}[AZSnI_3] - E_{tot}[AZI] - E_{tot}[SnI_2] \quad (5)$$

The calculated ΔH_d values are −91, −98, and −99 meV per formula unit (f.u.), respectively. These negative ΔH_d values indicate that all three types of $AZSnI_3$ will not decompose spontaneously. For $MAPbI_3$, the ΔH_d values reported in the literature for the decomposition reaction into MAI and PbI_2 secondary phases are largely energetically unfavored[30] and can even be decomposed spontaneously,[30,46,47] indicating that $MAPbI_3$ exhibits intrinsic thermal instability, which is consistent with the molecular dynamic calculation and the experimental results.[48,49] Therefore, the $AZSnI_3$ perovskites are expected to be more stable than the mainstream perovskite $MAPbI_3$. Here, we do not discuss whether the organic cation AZ can mitigate the oxidation of Sn^{2+} to Sn^{4+} in $AZSnI_3$. Nevertheless, one may calculate the decomposition energies of $AZSnI_3$, $MASnI_3$ and $FASnI_3$, in which the decomposition products have Sn^{4+}-based compounds, to evaluate whether AZ can mitigate the oxidation of Sn^{2+} to Sn^{4+}. Also, the chemical potential region (like Fig. 1(b)) can be adopted to evaluate whether AZ can mitigate the oxidation of Sn^{2+} to Sn^{4+} from the area of Sn^{4+}-based compounds in the region.

Materials with ABX_3 composition can adapt different crystal structures depending on the size and interaction of cation A and the corner-sharing BX_6 octahedral. Goldschmidt tolerance factor (t) is a reliable empirical index to predict which structure is preferentially formed.[50] The Goldschmidt tolerance factor is calculated from the ionic radius of the atoms using the following expression:

$$t = \frac{r_A + r_X}{\sqrt{2}(r_B + r_X)}$$

where r_A is the radius of cation A, r_B is the radius of cation B, and r_X is the radius of the anion. According to an earlier report,[4] a cubic perovskite structure can be formed when t is around 0.95 but not exceeding 1. For the $AZSnI_3$ structure, A is the organic AZ^+, generally with r_A = 2.27 Å;[30] X is the halogen anion, where we adopt r_I = 2.2 Å to get a reasonable t. Cation B is Sn here with r_B = 1.12 Å, and thus leading to a calculated factor of 0.95, which is substantially suitable for the cubic perovskite structure. Consequently, we adopt cubic $AZSnI_3$ with space group $Pm\bar{3}m$ in the following study and the optimized stable structure is shown in Fig. 1(a). The calculated lattice constants are $a = b = c$ = 6.34 Å.

Under thermodynamic equilibrium growth conditions, the chemical potentials are constrained in ranges that promote the growth of $AZSnI_3$ and exclude the formation of secondary phases, such as SnI_2 and AZI. Therefore, the chemical potentials should satisfy

$$\mu_{AZ} + \mu_{Sn} + 3\mu_I = \Delta H(AZSnI_3)(-5.11\ eV) \quad (6)$$

where μ_i is the chemical potential of the constituent element referred to as its most stable phase and $\Delta H(AZSnI_3)$ is the formation enthalpy of $AZSnI_3$. For μ_{AZ}, we choose face-centered-cubic phase of AZ following bulk Cs. To exclude the possible secondary phase SnI_2 and AZI (rock-salt phase), the following constraints must also be satisfied

$$\mu_{AZ} + \mu_I < \Delta H(AZI)(-3.26\ eV) \quad (7)$$

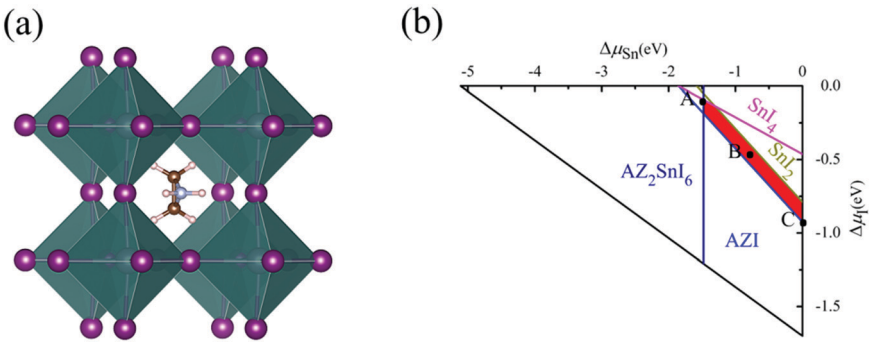

Fig. 1 (a) Schematic perovskite structure of $AZSnI_3$. (b) Calculated chemical ranges for forming AZI, SnI_2, and $AZSnI_3$ (middle red region). Three representative points A (μ_I = −0.09 eV, μ_{Sn} = −1.48 eV, μ_{AZ} = −3.63 eV), B (μ_I = −0.93 eV, μ_{Sn} = 0 eV, μ_{AZ} = −2.32 eV), and C (μ_I = −0.47 eV, μ_{Sn} = −0.74 eV, μ_{AZ} = −2.96 eV) are used for further investigation of defect properties.

$$\mu_{Sn} + 2\mu_I < \Delta H(SnI_2)(-1.58\ eV) \quad (8)$$

The chemical potentials of Sn and I satisfying eqn (6)–(8) are illustrated in the red region of Fig. 1(b), in which $AZSnI_3$ is stable against possible competing phases including AZI and SnI_2. The stable chemical potential window for $AZSnI_3$ has a long but narrow shape, typical for halide perovskites, indicating that the chemical growth condition should be carefully controlled to form pure $AZSnI_3$.

3.2. Electronic properties

The band structure is important for determining many physical properties, such as the absorption and effective mass of carriers, which are crucial for evaluating a new material for potential solar cell applications. The calculated band structure of $AZSnI_3$ using the HSE06 functional with 0.30 of exchange potential is displayed in the left panel of Fig. 2. Overall, the band structure is quite similar to that of cubic $MAPbI_3$, where the conduction band minimum (CBM) and VBM are located at the *R* point with a gap of 1.06 eV. To further understand the electronic structure of $AZSnI_3$, the density of states (DOS) are plotted in the right panel of Fig. 2. From the projected DOS (PDOS), the organic cation AZ has little contribution to the bands around VBM and CBM, resembling the case of other organic halide perovskites. VBM is mainly contributed by I 5p-orbitals and Sn 5s-orbitals, forming strong anti-bonding coupling, while CBM is contributed by Sn 5p. These electronic-structure features are similar to those of $MASnI_3$,[51] another prototype Sn-based perovskite that has gained increasing attention in the photovoltaic field. Both conduction and valence band edges exhibit dispersive bands, suggesting small carrier effective masses, which are turned to be 0.35 m_0, and 0.23 m_0 for electrons and holes, respectively.

For a single p–n junction on an AM 1.5 solar spectrum, the maximum theoretical efficiency of a solar cell is 33.7%, a value known as the Shockley–Queisser limit.[28] The electronic band gap of the absorber material is one of the key quantities to assure high efficiency for a solar cell. Ideally, the band gap value should be within the optimal range of 1.1–1.45 eV in order to approach the maximum theoretical efficiency. As mentioned above, the band gap of $AZSnI_3$ (1.06 eV), however, is slightly lower than the optimal band gap. Alloying with isovalent elements has been successfully used to tune the band gaps of solar cell absorbers, such as $MA(Sn,Pb)I_3$ and $CsSn(I,Br)_3$.[52–54] As the conduction and valence bands are derived mainly from the Sn 5p, as well as I 5p and Sn 5s states, respectively, the band gap of $AZSnI_3$ can be raised by alloying with isovalent elements that exhibit either p states higher in energy than Sn 5p or s states lower in energy than I 5p states. Considering the atomic size and electronegativity mismatch, Pb and Br are the first choices for alloying $AZSnI_3$. Pb, however, possesses a toxic character. Instead, Br is selected for alloying $AZSnI_3$ here. The calculated band gaps of $AZSnI_{3-x}Br_x$ using the HSE06 functional are shown in Fig. 3a. For each composition, various configurations with Br occupying different I sites have been considered, but only the lowest-energy configuration was chosen for band gap calculations. It is seen that alloying with Br can increase the band gap of $AZSnI_3$ effectively, as it increases almost linearly with the Br concentration. It should be noted that the change of Sn–I bond length in alloy $AZSnI_{3-x}Br_x$ is not linear, whereas the average Sn–I bond length in $AZSnI_3$, $AZSnI_2Br$ and $AZSnIBr_2$ is 3.01 Å, 3.07 Å and 3.22 Å. It leads to the band gap increase with Br content which is not linear. As shown in Fig. 3b, $AZSnI_2Br$ possesses a direct band gap of 1.31 eV, making it an optimal candidate for the light-absorber layer in single-junction perovskite solar cells following the Shockley–Queisser limit for single junction solar cells. Both the CBM and VBM of $AZSnI_2Br$ are localized at point R. From the PDOS, it is clear that VBM is predominantly contributed by I 5p-orbitals and Sn 5s-orbitals, as well a very small amount of Br 5p-orbitals, while the CBM is predominantly contributed by Sn 5p-orbitals. $AZSnI_2Br$ exhibits a similar band structure and DOS as $AZSnI_3$, except for its ideal band gap. Besides, the band edges of the valence band and conduction band are rather dispersive, expecting good carrier mobility like $AZSnI_3$. In fact, the calculated effective masses are 0.65 m_0 and 0.26 m_0 for electrons and holes, respectively.

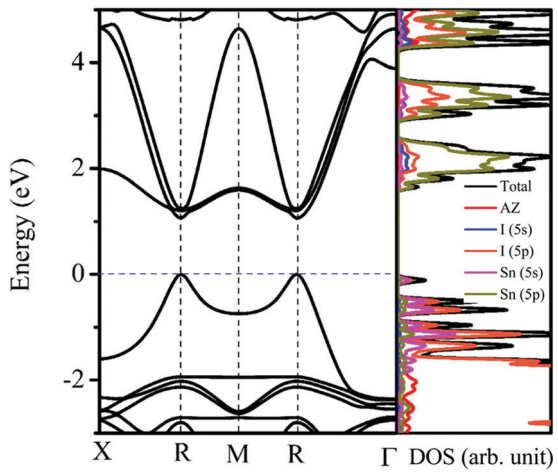

Fig. 2 Computed band structure and projected DOS of the $AZSnI_3$ using the HSE06 functional with 0.30 of exchange potential. Here, the VBM is set to zero.

Optical absorption is another important criterion for solar-cell materials. Apart from ambipolar conductivity, high optical absorption is one of the unique properties of hybrid perovskites, in which photon-generated carriers do not have to travel far in absorber layers to be collected at the contacts so that the nonradiative recombination rate is low. Fig. 3c shows calculated absorption spectra of $AZSnI_{3-x}Br_x$ in comparison with the typical perovskite $MAPbI_3$. It shows that $AZSnI_3$ has the maximum optical absorption in the entire visible solar spectrum in the studied systems. The results agree well with an earlier study,[27] where the optical absorption of Sn–I perovskites was reported to be stronger than that of Pb–I counterparts. With increasing I/Br ratio, the absorption is continuously red-shifted, consistent with the trend of band gap change. In addition, we find that the optical absorption coefficients of $AZSnI_{3-x}Br_x$ are even higher than that of $MAPbI_3$, as shown in

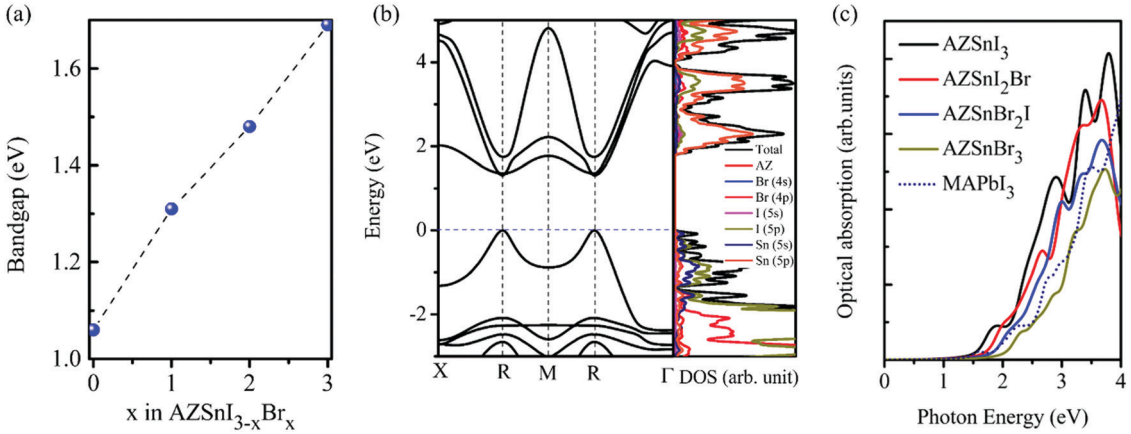

Fig. 3 (a) Calculated band gaps of $AZSnI_{3-x}Br_x$ alloys, and (b) the band structure and DOSs of $AZSnI_2Br$, as well as (c) the optical absorption coefficients of $AZSnI_3$, alloys $AZSnI_{3-x}Br_x$ and $MAPbI_3$, respectively.

Fig. 3c. As a result, $AZSnI_3$ and $AZSnI_{3-x}Br_x$ alloy perovskite devices are able to use even thinner absorbers to achieve high efficiencies, relative to the mainstream perovskite $MAPbI_3$. The choices of absorbers with ultrahigh optical absorption are particularly beneficial to cell performance as strong absorption ensures the harvesting of enough sunlight with extremely thin layers, thus shortening the diffusion length of the photoexcited carriers. This can effectively reduce the nonradiative recombination and enhance the open circuit voltages of the associated solar cells.

It is well known that large static dielectric constants can effectively screen the interaction between carriers and charged defects and impurities, thus improving the carrier lifetime and diffusion length. Here, the static dielectric constants for $AZSnI_3$ and $AZSnI_2Br$ are calculated. The calculated result of $AZSnI_3$ is $\varepsilon_{\text{eff}}^{xx} = 29.72$, $\varepsilon_{\text{eff}}^{yy} = 30.77$ and $\varepsilon_{\text{eff}}^{zz} = 56.42$. The result in $AZSnI_2Br$ is $\varepsilon_{\text{eff}}^{xx} = 96.39$, $\varepsilon_{\text{eff}}^{yy} = 7.44$ and $\varepsilon_{\text{eff}}^{zz} = 10.02$. Our calculated result shows that the values of static dielectric constants for $AZSnI_3$ and $AZSnI_2Br$ are comparable to that of $MAPbI_3$,[55] which suggests that $AZSnI_3$ and $AZSnI_2Br$ have excellent carrier transport properties like in $MAPbI_3$.

3.3. Defect properties

Solar cell performance depends critically on the defect properties of the light absorbers. To optimize the performance, it is important to find growth conditions that suppress the formation of the unwanted deep-level defects and promote the desirable defects. We have calculated the transition energy levels and formation energies of intrinsic point defects in $AZSnI_3$. These results also provide a reference to the defect properties in $AZSnI_{3-x}Br_x$ alloys.

We have considered 12 possible intrinsic point defects in $AZSnI_3$, including three vacancies (V_{AZ}, V_{Sn}, V_I), three interstitials (AZ_i, Sn_i, I_i), two cation substitutions (AZ_{Sn}, Sn_{AZ}), and four antisite substitutions (AZ_I, Sn_I, I_{AZ} and I_{Sn}). The calculated transition energies of these point defects are shown in Fig. 4. The donor-like defects are marked in red as shown in Fig. 4a, while the acceptor-like defects are in blue as shown in Fig. 4b. Only four

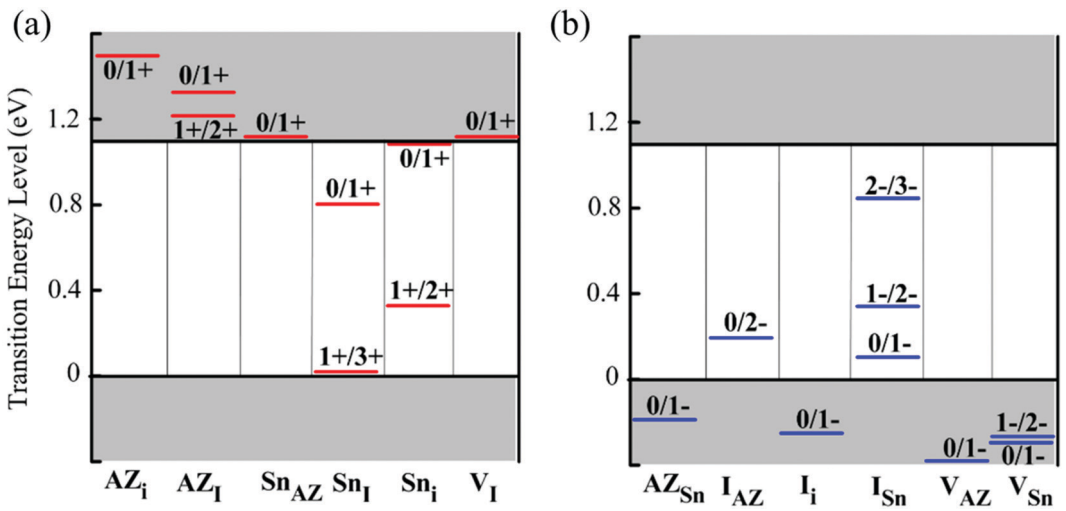

Fig. 4 Calculated transition energy levels of intrinsic defects in $AZSnI_3$. The red and blue bars represent the donor levels (a) and acceptor levels (b), respectively.

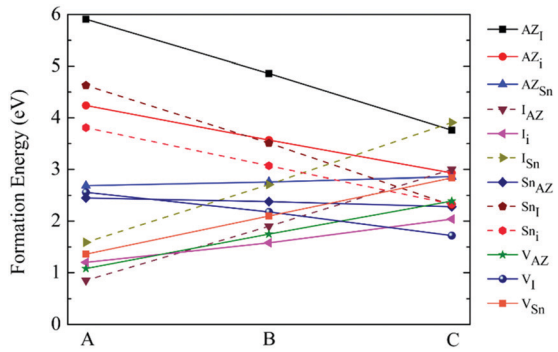

Fig. 5 Calculated formation energies of charge-neutral defects in $AZSnI_3$ as a function of chemical potential, where the detailed chemical potential values corresponding to A, B, C are shown in Fig. 1b.

defects (Sn_I, Sn_i, I_{AZ}, I_{Sn}) produce deep levels. Other point defects produce shallow levels: AZ_i, AZ_I, Sn_{AZ}, and V_I are shallow donors, whereas AZ_{Sn}, I_i, V_{AZ} and V_{Sn} are shallow acceptors.

The formation energies of point defects depend on the chemical potentials of the constituent elements. We have selected three representative chemical potential points, *i.e.*, different growth conditions for calculating the formation energies of point defects: A (I-rich/Sn-poor), B (moderate), and C (I-poor/Sn-rich), which are marked in Fig. 1b. We first calculated the formation energies for charge-neutral defects as a function of chemical potentials, as shown in Fig. 5. The solid lines indicate defects with shallow levels, whereas the dotted lines show defects with deep levels. It is seen that, at chemical point A (I-rich/Sn-poor), the defect with deep level, I_{AZ} exhibits the lowest formation energies. At chemical potential point C (I-poor/Sn-rich), the defect with shallow level, V_I exhibits the lowest formation energies.

The p/n electrical conductivity of a semiconductor is determined by the Fermi-level position, which is pinned by the most stable charged acceptor and donor defects in the system. We have calculated the formation energies of the above point defects as a function of Fermi-level position at three representative chemical potential points-A (I-rich/Sn-poor), B (moderate), and C (I-poor/Sn-rich). The results are shown in Fig. 6a–c. Defects with relatively high formation energies are indicated with dashed lines, while solid lines are for defects with relatively low formation energies. At chemical potential points A and B, the Fermi-level positions are pinned below the VBM, indicating degenerate p-type conductivity. At chemical potential point C, however, the Fermi-level position is pinned at 0.33 eV above the VBM by the formation of V_{Sn} and V_I, indicating moderate p-type conductivity.

Therefore, $AZSnI_3$ perovskite films grown under conditions of I-rich/Sn-poor and moderate are expected to be strong p-type semiconductors. High carrier concentration is preferred for contact layers but not for absorbers due to the high recombination of minority carriers. Our results suggest that I-poor/Sn-rich growth conditions may be applicable for synthesizing $AZSnI_3$-based perovskite absorbers as the formation of deep-level defects can be suppressed, and the carrier density can be maintained at moderate levels.

3.4. Stability of $AZSnI_{3-x}Br_x$ alloys

We have further studied the stability of $AZSnI_{3-x}Br_x$ alloys by calculating the energies needed to decompose the alloys back to the binary phases, such as AZI, AZBr, SnI_2 and $SnBr_2$ or the ternary phases $AZSnI_3$ and $AZSnBr_3$. The decomposition energies are defined as positive energies that do not favor energetic decomposition of the alloy:

$$E_d(B) = (3 - x)E_{total}(AZI) + xE_{total}(AZBr) + xE_{total}(SnBr_2) + (3 - x)E_{total}(SnI_2) - 3E_{total}AZSn(I_{3-x}Br_x) \quad (9)$$

$$E_d(T) = (3 - x)(AZSnI_3) + x(AZSnBr_3) - 3AZSn(I_{3-x}Br_x) \quad (10)$$

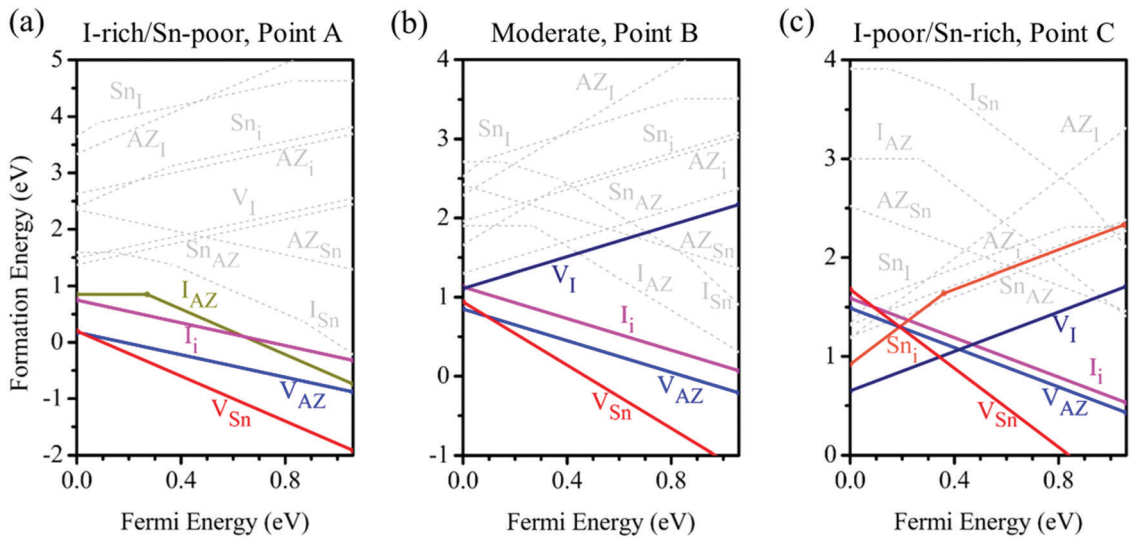

Fig. 6 Calculated formation energies of intrinsic point defects as a function of the Fermi level at three representative chemical potential points: (a) A (I-rich/Sn-poor), (b) B (moderate), and (c) C (I-poor/Sn-rich).

Table 1 Calculated decomposition energies for $AZSnI_{3-x}Br_x$ alloys

$AZSnI_{3-x}Br_x$	Binary (eV)	Ternary (eV)
$AZSnI_3$	0.091	—
$AZSnI_2Br$	0.781	−0.015
$AZSnIBr_2$	0.719	−0.044
$AZSnBr_3$	0.290	—

Here, B and T indicate the decompositions into binary and ternary secondary phases, respectively. E_{total} is the calculated total energy of a considered unit cell. As listed in Table 1, the alloys $AZSnI_{3-x}Br_x$ do not decompose into binary phases. The calculated decomposition energies, however, are negative when decomposing into the ternary phases, although the values are rather small, indicating a weak segregation trend in the alloys. Nevertheless, Yan *et al.* reported that unstable alloys may be synthesized under nonequilibrium growth or compressively strained growth conditions.[56]

Moreover, the stability of the compounds depends on temperature, which affects the entropy contribution due to mixed configurations and lattice vibrations. Herein, we calculate the entropy of mixing using the following equation:

$$\Delta S = -k_B[x\ln(x) + (1-x)\ln(1-x)] \quad (11)$$

The maximum contribution of mixing entropy (corresponding to $x = 0.5$) to the Helmholtz energy at room temperature is about −17.3 meV per atom, which will be beneficial for the stability of multi-component alloys. In general, the lattice vibration contribution to the ternary compound should be considered for binary decomposition energy. In our study, however, it takes huge computational resources to complete the phonon spectrum calculations for the compounds in different ratios. We noticed from the earlier study[57] that the phonon spectrums are similar for $Cs_{1-x}Rb_xPbI_3$ ($Cs_{1-x}Rb_xI$) with x = 0, 0.2, 0.6, 0.8, and 1.0. This implies that the contributions of lattice vibration to the decomposition energy will mostly be canceled out. Therefore, we expect that our estimation of decomposition without the consideration of the lattice vibration is reasonable.

4. Conclusions

To summarize, we propose the tin-based lead-free halide perovskite $AZSnI_3$ as well as alloys $AZSnI_{3-x}Br_x$, for stable and high-performance photovoltaic absorber materials. We find that the perovskite $AZSnI_3$ has much better stability than mainstream $MAPbI_3$ and possesses a band gap of 1.06 eV. Furthermore, it is found that I-poor/Sn-rich growth conditions are appropriate to suppress the formation of deep-level defects when synthesizing $AZSnI_3$-based perovskite absorbers to maintain moderate carrier density. In addition, the alloy $(CH_2)_2NH_2SnI_2Br$ has an ideal band gap of 1.31 eV, which is optimal for single junction solar cells. The calculated optical absorption of alloys $AZSnI_{3-x}Br_x$ is mostly higher than $MAPbI_3$.

Conflicts of interest

The authors declare no conflict of interest.

Acknowledgements

This work is financially supported by the NSFC (Grant No. 12074126), the Foundation for Innovative Research Groups of the National Natural Science Foundation of China (Grant No. 51621001), the Fundamental Research Funds for the Central Universities (Grant No. 2020ZYGXZR076), and the Natural Science Foundation of Guangdong Province of China (Grant No. 2016A030312011).

References

1 National Renewable Energy Laboratory, Best ResearchCell Efficiency Chart, 2020; www.nrel.gov/pv/cellefficiency.html.
2 A. Kojima, K. Teshima, Y. Shirai and T. Miyasaka, Organometal Halide Perovskites as Visible-Light Sensitizers for Photovoltaic Cells, *J. Am. Chem. Soc.*, 2009, **131**(17), 6050–6051.
3 T. A. Berhe, W. N. Su, C. H. Chen, C. J. Pan, J. H. Cheng, H. M. Chen and B. J. Hwang, Organometal halide perovskite solar cells: degradation and stability, *Energy Environ. Sci.*, 2016, **9**(2), 323–356.
4 Z. Li, M. Yang, J. S. Park, S. H. Wei, J. J. Berry and K. Zhu, Stabilizing perovskite structures by tuning tolerance factor: formation of formamidinium and cesium lead iodide solid-state alloys, *Chem. Mater.*, 2016, **28**(1), 284–292.
5 B. Charles, J. Dillon, O. J. Weber, M. S. Islam and M. T. Weller, Understanding the stability of mixed A-cation lead iodide perovskites, *J. Mater. Chem. A*, 2017, **5**(43), 22495–22499.
6 M. Saliba, T. Matsui, J. Y. Seo, K. Domanski, J. P. Correa-Baena, M. K. Nazeeruddin and M. Grätzel, Cesium-containing triple cation perovskite solar cells: improved stability, reproducibility and high efficiency, *Energy Environ. Sci.*, 2016, **9**(6), 1989–1997.
7 N. K. Noel, S. D. Stranks, A. Abate, C. Wehrenfennig, S. Guarnera, A.-A. Haghighirad, A. Sadhanala, G. E. Eperon, S. K. Pathak and M. B. Johnston, Lead-free organic–inorganic tin halide perovskites for photovoltaic applications, *Energy Environ. Sci.*, 2014, **7**(9), 3061–3068.
8 F. Wang, J. Ma, F. Xie, L. Li, J. Chen, J. Fan and N. Zhao, Organic Cation-Dependent Degradation Mechanism of Organotin Halide Perovskites, *Adv. Funct. Mater.*, 2016, **26**(20), 3417–3423.
9 N. Wang, Y. Y. Zhou, M. G. Ju, H. F. Garces, T. Ding, S. P. Pang, X. C. Zeng, N. P. Padture and X. W. Sun, Heterojunction-Depleted Lead-Free Perovskite Solar Cells with Coarse-Grained B-γ-$CsSnI_3$ Thin Films, *Adv. Energy Mater.*, 2016, **6**(24), 1601130.
10 Z. Yang, A. Rajagopal, C. C. Chueh, S. B. Jo, B. Liu, T. Zhao and A. K. Y. Jen, Stable Low-Bandgap Pb–Sn Binary

Perovskites for Tandem Solar Cells, *Adv. Mater.*, 2016, **28**(40), 8990–8997.

11 Y. L. Li, W. H. Sun, W. B. Yan, S. Ye, H. Rao, H. Peng, Z. Zhao, Z. Bian, Z. Liu and H. Zhou, 50% Sn-Based Planar Perovskite Solar Cell with Power Conversion Efficiency up to 13.6%, *Adv. Energy Mater.*, 2016, **6**(24), 1601353.

12 G. H. Xing, M. H. Kumar, W. K. Chong, X. Liu, Y. Cai, H. Ding, M. Asta, M. Grätzel, S. Mhaisalkar and N. Mathews, Solution-Processed Tin-Based Perovskite for Near-Infrared Lasing, *Adv. Mater.*, 2016, **28**(37), 8191–8196.

13 A. Babayigit, A. Ethirajan, M. Muller and B. Conings, Toxicity of organometal halide perovskite solar cells, *Nat. Mater.*, 2016, **15**(3), 247.

14 A. Babayigit, D. D. Thanh, A. Ethirajan, J. Manca, M. Muller, H. G. Boyen and B. Conings, Assessing the toxicity of Pb-and Sn-based perovskite solar cells in model organism Danio rerio, *Sci. Rep.*, 2016, **6**(1), 1–11.

15 G. Nasti and A. Abate, Tin Halide Perovskite ($ASnX_3$) Solar Cells: A Comprehensive Guide toward the Highest Power Conversion Efficiency, *Adv. Energy Mater.*, 2020, **10**(13), 1902467.

16 J. Li, H. L. Cao, W. B. Jiao, Q. Wang, M. Wei, I. Cantone and A. Abate, Biological impact of lead from halide perovskites reveals the risk of introducing a safe threshold, *Nat. Commun.*, 2020, **11**(1), 1–5.

17 F. Hao, C. C. Stoumpos, D. H. Cao, R. P. Chang and M. G. Kanatzidis, Lead-free solid-state organic–inorganic halide perovskite solar cells, *Nat. Photonics*, 2014, **8**(6), 489.

18 Y. Li, W. Sun, W. Yan, S. Ye, H. Rao, H. Peng, Z. Zhao, Z. Bian, Z. Liu and H. Zhou, 50% Sn-Based Planar Perovskite Solar Cell with Power Conversion Efficiency up to 13.6%, *Adv. Energy Mater.*, 2016, **6**(24), 1601353.

19 W. Q. Liao, D. W. Zhao, Y. Yu, C. R. Grice, C. Wang, A. J. Cimaroli, P. Schulz, W. Meng, K. Zhu and R. G. Xiong, Lead-free inverted planar formamidinium tin triiodide perovskite solar cells achieving power conversion efficiencies up to 6.22%, *Adv. Mater.*, 2016, **28**(42), 9333–9340.

20 S. J. Lee, S. S. Shin, Y. C. Kim, D. Kim, T. K. Ahn, J. H. Noh, J. Seo and S. I. Seok, Fabrication of efficient formamidinium tin iodide perovskite solar cells through SnF_2–pyrazine complex, *J. Am. Chem. Soc.*, 2016, **138**(12), 3974–3977.

21 T. Yokoyama, D. H. Cao, C. C. Stoumpos, T.-B. Song, Y. Sato, S. Aramaki and M. G. Kanatzidis, Overcoming short-circuit in lead-free $CH_3NH_3SnI_3$ perovskite solar cells via kinetically controlled gas–solid reaction film fabrication process, *J. Phys. Chem. Lett.*, 2016, **7**(5), 776–782.

22 F. Hao, C. C. Stoumpos, P. J. Guo, N. J. Zhou, T. J. Marks, R. P. Chang and M. G. Kanatzidis, Solvent-mediated crystallization of $CH_3NH_3SnI_3$ films for heterojunction depleted perovskite solar cells, *J. Am. Chem. Soc.*, 2015, **137**(35), 11445–11452.

23 W. Liao, D. Zhao, Y. Yu, C. R. Grice, C. Wang, A. J. Cimaroli, P. Schulz, W. Meng, K. Zhu and R. G. Xiong, Lead-free inverted planar formamidinium tin triiodide perovskite solar cells achieving power conversion efficiencies up to 6.22%, *Adv. Mater.*, 2016, **28**(42), 9333–9340.

24 Q. Tai, X. Guo, G. Tang, P. You, T. W. Ng, D. Shen, J. Cao, C. K. Liu, N. Wang and Y. Zhu, Antioxidant Grain Passivation for Air-Stable Tin-Based Perovskite Solar Cells, *Angew. Chem., Int. Ed.*, 2019, **58**(3), 806–810.

25 I. Chung, J.-H. Song, J. Im, J. Androulakis, C. D. Malliakas, H. Li, A. J. Freeman, J. T. Kenney and M. G. Kanatzidis, $CsSnI_3$: semiconductor or metal? High electrical conductivity and strong near-infrared photoluminescence from a single material. High hole mobility and phase-transitions, *J. Am. Chem. Soc.*, 2012, **134**(20), 8579–8587.

26 T. T. Shi, H. S. Zhang, W. W. Meng, Q. Teng, M. Liu, X. Yang, Y. Yan, H.-L. Yip and Y.-J. Zhao, Effects of organic cations on the defect physics of tin halide perovskites, *J. Mater. Chem. A*, 2017, **5**(29), 15124–15129.

27 C. C. Stoumpos, C. D. Malliakas and M. G. Kanatzidis, Semiconducting tin and lead iodide perovskites with organic cations: phase transitions, high mobilities, and near-infrared photoluminescent properties, *Inorg. Chem.*, 2013, **52**(15), 9019–9038.

28 W. Shockley and H. J. Queisser, Detailed Balance Limit of Efficiency of p–n Junction Solar Cell, *J. Appl. Phys.*, 1961, **32**(3), 510.

29 C. Zheng and O. Rubel, Ionization energy as a stability criterion for halide perovskites, *J. Phys. Chem. C*, 2017, **121**(22), 11977–11984.

30 C. Zheng and O. Rubel, Aziridinium lead iodide: a stable, low-band-gap hybrid halide perovskite for photovoltaics, *J. Phys. Chem. Lett.*, 2018, **9**(4), 874–880.

31 G. Kresse and J. Furthmüller, Efficient iterative schemes for *ab initio* total-energy calculations using a plane-wave basis set, *Phys. Rev. B: Condens. Matter Mater. Phys.*, 1996, **54**(16), 11169–11186.

32 G. Kresse and J. Furthmüller, Efficiency of *ab initio* total energy calculations for metals and semiconductors using a plane-wave basis set, *Comput. Mater. Sci.*, 1996, **6**(1), 15–50.

33 G. Kresse and D. Joubert, From ultrasoft pseudopotentials to the projector augmented-wave method, *Phys. Rev. B: Condens. Matter Mater. Phys.*, 1999, **59**(3), 1758–1775.

34 J. P. Perdew, K. Burke and M. Ernzerhof, Generalized Gradient Approximation Made Simple, *Phys. Rev. Lett.*, 1996, **77**(18), 3865–3868.

35 J. R. Li and P. Rinke, Atomic structure of metal-halide perovskites from first principles: the chicken-and-egg paradox of the organic-inorganic interaction, *Phys. Rev. B*, 2016, **94**(4), 045201.

36 G. Stefan, A. Jens, E. Stephan and K. Helge, A consistent and accurate *ab initio* parametrization of density functional dispersion correction (DFT-D) for the 94 elements H-Pu, *J. Chem. Phys.*, 2010, **132**(15), 154104.

37 H. J. Monkhorst and J. D. Pack, Special points for Brillouin-zone integrations, *Phys. Rev. B: Condens. Matter Mater. Phys.*, 1976, **13**(12), 5188–5192.

38 J. Paier, M. Marsman, K. Hummer, G. Kresse, I. C. Gerber and J. G. Ángyán, Screened hybrid density functionals applied to solids, *J. Chem. Phys.*, 2006, **124**(15), 154709.

39 K. Shum, Z. Chen, J. Qureshi, C. L. Yu, J. J. Wang, W. Pfenninger, N. Vockic, J. Midgley and J. T. Kenney,

Synthesis and characterization of $CsSnI_3$ thin films, *Appl. Phys. Lett.*, 2010, **96**(22), 221903.

40 Z. Chen, C. L. Yu, K. Shum, J. J. Wang, W. Pfenninger, N. Vockic, J. Midgley and J. T. Kenney, Photoluminescence study of polycrystalline $CsSnI_3$ thin films: Determination of exciton binding energy, *J. Lumin.*, 2012, **132**(2), 345–349.

41 S. Saha, T. P. Sinha and A. Mookerjee, Electronic structure, chemical bonding, and optical properties of paraelectric $BaTiO_3$, *Phys. Rev. B: Condens. Matter Mater. Phys.*, 2000, **62**(13), 8828–8834.

42 S. Lany and A. Zunger, Assessment of correction methods for the band-gap problem and for finite-size effects in supercell defect calculations: Case studies for ZnO and GaAs, *Phys. Rev. B: Condens. Matter Mater. Phys.*, 2008, **78**(23), 235104.

43 T. Leijtens, K. Bush, R. R. Cheacharoen, R. Beal, A. Bowring and M. D. McGehee, Towards enabling stable lead halide perovskite solar cells; interplay between structural, environmental, and thermal stability, *J. Mater. Chem. A*, 2017, **5**(23), 11483–11500.

44 J. Burschka, N. Pellet, S.-J. Moon, R. Humphry-Baker, P. Gao, M. K. Nazeeruddin and M. Grätzel, Sequential deposition as a route to high-performance perovskite-sensitized solar cells, *Nature*, 2013, **499**, 316.

45 G. D. Niu, W. Z. Li, F. Q. Meng, L. Wang, H. Dong and Y. Qiu, Study on the stability of $CH_3NH_3PbI_3$ films and the effect of post-modification by aluminum oxide in all-solid-state hybrid solar cells, *J. Mater. Chem. A*, 2014, **2**(3), 705–710.

46 Y.-Y. Zhang, S. Chen, P. Xu, H. Xiang, X.-G. Gong, A. Walsh and S.-H. Wei, Intrinsic Instability of the Hybrid Halide Perovskite Semiconductor $CH_3NH_3PbI_3$, *Chin. Phys. Lett.*, 2018, **35**(3), 036104.

47 A. M. Ganose, C. N. Savory and D. O. Scanlon, $CH_3NH_3)_2Pb(SCN)_2I_2$: A More Stable Structural Motif for Hybrid Halide Photovoltaics?, *J. Phys. Chem. Lett.*, 2015, **6**(22), 4594–4598.

48 E. Mosconi, J. M. Azpiroz and F. De Angelis, *Ab Initio* Molecular Dynamics Simulations of Methylammonium Lead Iodide Perovskite Degradation by Water, *Chem. Mater.*, 2015, **27**(13), 4885–4892.

49 B. Conings, J. Drijkoningen, N. Gauquelin, A. Babayigit, J. D'Haen, L. D'Olieslaeger, A. Ethirajan, J. Verbeeck, J. Manca, E. Mosconi, F. D. Angelis and H.-G. Boyen, Intrinsic Thermal Instability of Methylammonium Lead Trihalide Perovskite, *Adv. Energy Mater.*, 2015, **5**(15), 1500477.

50 V. M. Goldschmidt, Die gesetze der krystallochemie, *Naturwissenschaften*, 1926, **14**(21), 477–485.

51 P. P. Sun, Q. S. Li, L. N. Yang and Z. S. Li, Theoretical insights into a potential lead-free hybrid perovskite: substituting Pb^{2+} with Ge^{2+}, *Nanoscale*, 2016, **8**(3), 1503–1512.

52 Y. H. Ogomi, A. Morita, S. Tsukamoto, T. Saitho, N. Fujikawa, Q. Shen, T. Toyoda, K. Yoshino, S. S. Pandey, T. Ma and S. Hayase, $CH_3NH_3Sn_xPb_{1-x}I_3$ Perovskite Solar Cells Covering up to 1060 nm, *J. Phys. Chem. Lett.*, 2014, **5**(6), 1004–1011.

53 D. Sabba, H. K. Mulmudi, R. R. Prabhakar, T. Krishnamoorthy, T. Baikie, P. P. Boix, S. Mhaisalkar and N. Mathews, Impact of Anionic Br-Substitution on Open Circuit Voltage in Lead Free Perovskite ($CsSnI_{3-}xBrx$) Solar Cells, *J. Phys. Chem. C*, 2015, **119**(4), 1763–1767.

54 L. Peedikakkandy and P. Bhargava, Composition dependent optical, structural and photoluminescence characteristics of cesium tin halide perovskites, *RSC Adv.*, 2016, **6**(24), 19857–19860.

55 M. H. Du, Efficient carrier transport in halide perovskites: theoretical perspectives, *J. Mater. Chem. A*, 2014, **2**(24), 9091–9098.

56 W. Meng, B. Saparov, F. Hong, J. Wang, D. B. Mitzi and Y. Yan, Alloying and defect control within chalcogenide perovskites for optimized photovoltaic application, *Chem. Mater.*, 2016, **28**(3), 821–829.

57 U. G. Jong, C. J. Yu, Y. H. Kye, Y. S. Kim, C. H. Kim and S. G. Ri, A first-principles study on the chemical stability of inorganic perovskite solid solutions $Cs_{1-x}Rb_xPbI_3$ at finite temperature and pressure, *J. Mater. Chem. A*, 2018, **6**(37), 17994–18002.

